



PtSn nanoparticles supported on titanium carbonitride for the ethanol oxidation reaction

M. Roca-Ayats^{a,*,}, O. Guillén-Villafuerte^c, G. García^{c,*}, M. Soler-Vicedo^b, E. Pastor^c, M.V. Martínez-Huerta^{b,*}

^a Physical Chemistry Department, Faculty of Chemistry, University of Santiago de Compostela, E-15782 Santiago de Compostela, Spain

^b Instituto de Catálisis y Petroleoquímica, CSIC, Marie Curie 2, E28049 Madrid, Spain

^c Instituto Universitario de Materiales y Nanotecnología, Universidad de La Laguna, c/ Astrofísico F. Sánchez, E38071 La Laguna, Tenerife, Spain



ARTICLE INFO

Keywords:

Platinum
Tin
Titanium carbonitride
Ethanol
Electrocatalysis

ABSTRACT

The effect of titanium carbonitride (TiCN) as a new support for platinum-tin nanoparticulated catalysts for the ethanol oxidation reaction (EOR) in acid medium was evaluated. For that purpose, two platinum-tin catalysts supported on TiCN and carbon black (Vulcan XC-72R) were synthesized following the ethylene glycol method. XRD, TEM, ICP-OES and XPS techniques revealed that both catalysts exhibit similar physicochemical properties. However, the EOR and the CO tolerance were enhanced at the catalyst supported on TiCN. *In situ* Fourier transform infrared spectroscopy (FTIR) and differential electrochemical mass spectrometry (DEMS) were used in order to get more information on the reaction mechanism and product selectivity. Main results indicate an improvement of the CO oxidation reaction by facile water dissociation on PtSn/TiCN, and elevated current output during the EOR on PtSn/TiCN since the acetaldehyde path is the favored, meanwhile the CO and acetic acid pathways are suppressed at this catalytic material. Significant differences were observed between both catalysts, indicating an extraordinary impact of the support in the catalytic performance.

1. Introduction

Direct ethanol fuel cells (DEFCs) are interesting devices for portable energy applications. Ethanol is a cheap fuel, non-toxic and with a high energy density per volume unit [1–3]. In addition, bio-ethanol can be considered a quasi-renewable energy, as it can be obtained from the conversion of sugars, biomass, cereals or other carbon-based feedstock. However, for the implementation of DEFCs some improvements need to be made regarding the Pt-based catalyst usually employed in these devices, which is expensive, low-abundance and it is not capable to completely oxidize ethanol to CO₂ at high rates [1,2].

The ethanol electrooxidation reaction (EOR) is a complex process which involves several intermediates and parallel pathways [4,5]. The complete oxidation of ethanol to CO₂ through the direct pathway involves the production of 12 electrons, C–C cleavage and further oxidation of adsorbed species (CO and CH_x) [6]. C–C has a low bonding energy, but its cleavage is not an easy process due to geometric impediments that leads to slow kinetics. On the other side, CO is known to be one of the main catalytic poisons, as it adsorbs strongly onto some

metal surfaces such as platinum. In addition to the direct pathway, ethanol can oxidize without the C–C cleavage, giving rise to adsorbed acetaldehyde. Acetaldehyde can desorb and get dissolved in the electrolyte or further oxidize to adsorbed acetate and acetic acid [4–6]. However, acetate adsorbs strongly on platinum surfaces, becoming, as well, a catalytic poison for the ethanol oxidation reaction [7,8]. C–C bond on acetaldehyde can also be broken forming adsorbed C₁ species (CO + CH_x) [4]. The oxidation of ethanol to acetaldehyde and acetic acid provides 2 and 4 electrons, respectively, decreasing considerably the efficiency of the process.

Several of the steps on the ethanol oxidation reaction need the formation of adsorbed hydroxyl groups. The decomposition of water, giving rise to adsorbed hydroxyl, takes place at high overpotentials on platinum surfaces. For that reason, the incorporation of a second metal able to activate water at lower overpotentials is recommended to make operative the bifunctional mechanism, and catalysts employed for ethanol oxidation are usually made of platinum alloyed nanoparticles supported on carbon materials. Metals such as tin, rhodium, iron, ruthenium, molybdenum and nickel are incorporated in the alloy in order

* Corresponding authors.

** Corresponding author. Current address: Battery an Electrochemistry Laboratory, Institute of Nanotechnology, Karlsruhe Institute of Technology, Hermann-von-Helmholtz-Platz 1, 76344 Eggenstein-Leopoldshafen, Germany.

E-mail addresses: maroay@gmail.com (M. Roca-Ayats), ggarci@ull.edu.es (G. García), mmartinez@icp.csic.es (M.V. Martínez-Huerta).

to get a better performance of the catalysts [9–14]. Among all of these, tin is the most employed one due to its interesting properties. The incorporation of tin may be in the form of platinum alloys, being Pt_3Sn the most common and active one, or non-alloyed phases (mainly SnO_2). However, for conventional electrocatalyst, it is common to obtain materials with a mixture of alloyed and non-alloyed phases (Pt_3Sn , Pt, SnO_2 ,...) [15]. Tin, specially in non-alloyed forms, can provide adsorbed hydroxyl groups at much lower overpotentials than platinum does, in the so called bifunctional mechanism, enhancing all reaction steps that involve this adsorbate. Thus, lower onset potentials and higher current densities are obtained. In addition, it has been reported that alloyed tin also causes an electronic effect (ligand effect) that favors the EOR on platinum [16,17]. However, it is also known that the presence of tin hinders the C–C cleavage, decreasing the process efficiency and increasing the acetic acid yields [18].

However, not much effort has been done in order to obtain catalytic supports that can act as promoters for the EOR. It is well known that transition metal oxides are hydrophilic compounds that can provide OH^- groups at small overpotentials [19]. Adsorbed oxygenated species on the surface of the catalyst support has been reported to affect positively the catalytic activity toward the EOR at both platinum and platinum-based catalysts [19–21]. However, most of the transition metal oxides are not electrical conductive enough to be used as fuel cell components. For that reason, other materials such as transition metal carbides (TMC) and nitrides (TMN) have been proposed as good candidates in order to replace carbon as catalyst support [22–24].

TMC and TMN are highly crystalline materials and possess high electrical conductivity and a strong resistance to corrosion and wear. In addition, they have an electronic structure near Fermi level quite similar of that of noble metals, which make them to interact strongly with metal nanoparticles supported on them [22]. Thus, TMC and TMN are commonly used as electrocatalyst supports [22,25–31]. They usually form covalent bonds with the nanoparticles, although the presence of a polarization of electrons around metallic gold clusters supported on TiC was also detected [32].

Among the whole family of TMC and TMN, titanium carbide (TiC) and titanium nitride (TiN) have attracted some attention due to their special stability. Titanium carbonitride (TiCN) appears to be a good candidate, as well, as it is a solid solution of TiC and TiN. It keeps the fcc crystalline structure and possesses improved mechanical properties [33]. In this sense, several works reporting the utilization of titanium carbides and nitrides as electrocatalyst supports can be found in literature [26,34–40], but less studies regarding the utilization of TiCN have been reported [41–44]. Concerning the utilization of these materials as catalyst supports for the electrooxidation of CO and alcohols, a promoting effect was observed in acid and alkaline media [34,35,37,42]. This promoting effect was ascribed to the presence of oxygenated species on the surface of the catalyst support, which was considerably enhanced when TiC and TiCN were electrochemical potential cycled up to 1.0 V vs. RHE, as the surface of these supports was further oxidized [45].

In the present work, the synergistic effect of TiCN as catalyst support was evaluated for platinum-tin nanoparticles and compared with similar metallic nanoparticles supported on carbon black. *In situ* Fourier transform infrared spectroscopy (FTIRS) and differential electrochemical mass spectrometry (DEMS) were used to evaluate the reaction mechanism of the EOR at both electrocatalysts and, consequently, to understand the crucial effect of the catalyst supports on the catalytic activity.

2. Experimental section

2.1. Catalysts synthesis

Platinum-tin nanoparticles supported on carbon black (Vulcan XC-72R, Cabot, surface area: $230 \text{ m}^2 \text{ g}^{-1}$) and titanium carbonitride

($\text{TiC}_{0.7}\text{N}_{0.3}$, Sigma-Aldrich, SA: $22 \text{ m}^2 \text{ g}^{-1}$) were synthesized following the ethylene glycol method [46]. Ethylene glycol (> 99%, Sigma-Aldrich) was used as solvent and reducing agent. Appropriate amounts of metal precursors (99.99% PtCl_4 and 99.98% anhydrous SnCl_2 , both from Alfa Aesar) were employed to obtain nominal metal loading of 20 wt.% with a Pt:Sn atomic ratio of 3:1 on the catalyst support. The one-pot synthesis method consisted in the addition of the metal precursors previously dispersed in ethylene glycol into a suspension of the catalyst support in the same solvent. Then, the pH was adjusted to 11 and the temperature increased to 160 °C under a N_2 flow. After 3 h, the pH was adjusted to 2 and the catalysts were washed with acetone and later rinsed with water and dried at 80 °C. Finally, a thermal treatment was carried out under He flow (80 mL min^{-1}) during 1 h at a 250 °C. Catalysts were labeled as PtSn/TiCN and PtSn/C .

2.2. Physicochemical characterization

Transmission electron microscopy images were obtained from a HRTEM JEOL 2100 F operating at 200 eV. Obtained images were used to evaluate the morphology and agglomeration degree, as well as to calculate the average nanoparticle sizes. For that purpose, the diameter of a minimum of 300 nanoparticles was determined.

Chemical composition of the catalysts was determined by an inductively coupled plasma optical emission spectrometry (ICP-OES), with a Perkin Elmer Optima 3300 DV spectrometer.

X-ray diffractograms were obtained on a PANalytical X'Pert Pro X-ray diffractometer with a Cu K α source. Bragg's angles ranging from 4° to 90° were recorded at a scan rate of 0.02° per second and with an accumulation time of 500 s.

X-ray Photoelectron Spectroscopy (XPS) data were obtained with a SPECS GmbH customized system for surface analysis equipped with a non-monochromatic X-ray source XR 50 and a hemispherical energy analyzer PHOIBOS 1509MCD. X-ray Mg K α line (1253.6 eV) was used as excitation (operating at 200 W/12 kV). Powder samples were attached onto Cu foil and were placed first in the pre-treatment chamber at room temperature for several hours before being transferred to the analysis chamber. The XPS data were signal averaged for enough number of scans to get a good signal/noise ratio, at increments of 0.1 eV and fixed pass energy of 25 eV. High-resolution spectra envelopes were obtained by curve fitting synthetic peak components using the software XPSpeak. The raw data were used with no preliminary smoothing. Symmetric Gaussian-Lorentzian product functions were used to approximate the line shapes of the fitting components. Binding energies were calibrated relative to the C 1s peak from the graphitic carbon at 284.6 eV.

2.3. Electrochemical characterization

All measurements were carried out in a three-electrode cell at room temperature controlled by an Autolab PGSTAT302 potentiostat-galvanostat. A glassy carbon rod was used as counter electrode while a reversible hydrogen electrode (RHE) in the supporting electrolyte was used as reference. The working electrode was prepared by depositing 20 μL of catalytic ink onto a glassy carbon (area 0.28 cm^2). Metal loading (Pt + Sn): $57 \mu\text{g cm}^{-2}$). The catalytic ink was prepared by sonicating 2 mg of catalyst with 15 μL Nafion® (5%, Sigma Aldrich) and 500 μL of ultrapure water (MilliQ, Millipore). 0.5 M H_2SO_4 (EMSURE® ISO, Merck) was used as electrolyte while 2 M $\text{CH}_3\text{CH}_2\text{OH}$ (HPLC grade, Scharlau) + 0.5 M H_2SO_4 solution was used to study the EOR. N_2 (99.999%, Air Liquide) was employed to deoxygenate all solutions and CO (99.997%, Air Liquide) for CO stripping experiments. Electrochemical activation of the electrode was performed by potential cycling between 0.05 and 0.9 V vs RHE at a scan rate of 0.1 V s^{-1} during 50 cycles. CO stripping experiments were recorded at 0.02 V s^{-1} after bubbling CO through the cell for 10 min while keeping the electrode at 0.10 V, followed by N_2 purging during 30 min to completely remove the

excess of CO. CO stripping voltammograms were recorded, by first scanning negatively until 0.05 V so that the entire hydrogen region was probed, and then scanning positively up to 0.9 V. Ethanol cyclic voltammograms (CVs) were recorded between 0.05 and 0.9 V at a scan rate of 0.02 V s^{-1} , while current transients were obtained by stepping the potential from 0.05 V to the final oxidation potential ($0.45 < E_f < 0.60 \text{ V}$). Tafel plots were calculated from stationary currents achieved at 600 s during the chronoamperometry experiments. Currents were normalized by the electroactive surface area (ESA) obtained from CO stripping experiments (2.56 cm^2 for PtSn/TiCN and 8.42 cm^2 for PtSn/C).

In situ Fourier transform Infrared spectroscopy (FTIRS) data were obtained using a NICOLET 6700 FTIR spectrometer equipped with a MCT detector and fitted with a PIKE Technologies VeeMAX II total reflection spectroscopic accessory. An external beam configuration was employed, where CaF_2 prism was placed at the bottom of the electrochemical cell, similar to the cell described elsewhere [47]. The working electrode was prepared by depositing catalytic ink on top of a polycrystalline gold disk electrode and it was pressed against the prism. In this way, a thin layer of the electrolyte or the working solution was stabilized between the working electrode and the prism. FTIRS spectra were acquired from the average of 32 spectra with a resolution of 4 cm^{-1} , applying 0.1 V single potential steps from a reference potential ($E_o = 0.1$ or 0.05 V) up to 1.0 V . The reflectance ratio R/R_o was calculated. In this way, positive and negative bands represent loss and formation of species, respectively. The ethanol concentration was 0.5 M for all FTIRS experiments.

Differential electrochemical mass spectrometry (DEMS) measurements were obtained with an electrochemical cell connected to a commercial mass spectrometer (Omnistar™, Pfeiffer). The cell was connected to the vacuum system through a PTFE capillary (Supelco) with a PTFE membrane (Gore-Tex) placed on its top. The capillary was fixed at the center of the glassy carbon working electrode, as described elsewhere [48]. DEMS technique was used to detect the volatile and gaseous intermediates and/or products of CO_{ads} and ethanol oxidation reactions. The experimental setup allows the simultaneous detection of mass spectrometric cyclic voltammograms (MSCVs) for a selected mass-to-charge ratio (m/z) and cyclic voltammograms (CVs). For ethanol oxidation experiments followed by DEMS, the ethanol concentration was 0.5 M .

3. Results and discussion

Two PtSn electrocatalysts supported on TiCN and carbon black, respectively, were synthesized and labeled as PtSn/TiCN and PtSn/C. A Pt:Sn ratio of 3:1 was chosen in order to favor the formation of a Pt_3Sn alloyed phase, as it has been reported to be highly active for the oxidation of ethanol [15]. The total metal loading of the catalysts was fixed to 20 wt% in order to avoid major agglomeration on the TiCN supported catalyst, as the surface area of this material is not as large as most carbon supports.

3.1. Physicochemical characterization

Fig. 1 shows the X-ray diffractograms obtained for the two PtSn catalysts synthesized. The main difference between both diffractograms is the great intensity of the TiCN material. This diffraction pattern corresponds with the typical f.c.c structure (JPCDS 00-042-1489) already reported for TiCN [42,49] that reveals the high crystallinity of the titanium-based support. The last makes difficult to accurately obtain the crystallite size value. The lattice parameter calculated for PtSn/C and PtSn/TiCN catalysts are 3.951 and 3.949 \AA , respectively. These values fall in between the lattice constant for pure platinum (3.9231 \AA , JPCDS 00-004-0802) and that of Pt_3Sn phase (4.0015 \AA , JPCDS 00-035-1360). The last indicates that both catalysts are a mixture of alloyed and non-alloyed Pt-Sn, forming different phases such as Pt_3Sn , Pt and

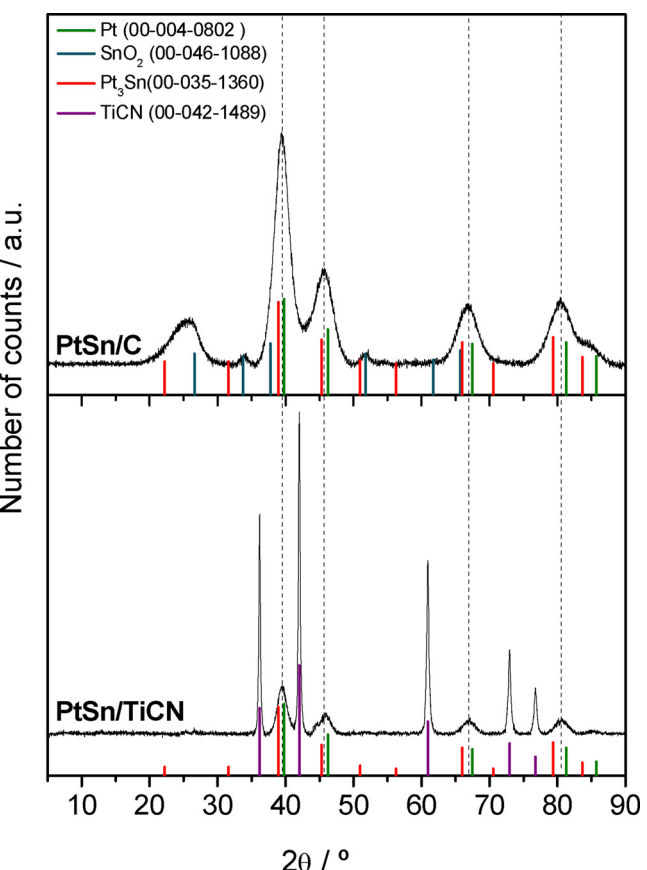


Fig. 1. XRD patterns of PtSn/C and PtSn/TiCN.

SnO_x . In fact, small diffraction profiles corresponding to SnO_2 are observed for the catalyst supported on carbon, but should not be discarded in the PtSn/TiCN diffractogram, as the high crystallinity of the support may hinder the signal.

The coexistence of different Pt-Sn phases may not negatively affect the catalytic activity. Even it has been reported that an increment in the alloying degree involves an enhancement of the catalytic activity toward the EOR, the presence of different phases and different Pt-Sn interactions may favor the development of different promoting mechanisms (e.g. ligand effect for alloyed Pt_3Sn and bifunctional mechanism for non-alloyed Pt-SnO_x) [17]. A lattice parameter of 3.956 \AA , not far from the values obtained in our catalysts, has been reported to be the optimum for EOR [50]. Nevertheless, the two catalysts synthesized present active phases with similar crystallographic properties and with almost the same percentage of alloyed and non-alloyed Pt-Sn phases with only a slightly higher alloying degree for the catalyst supported on carbon. In order to estimate the amount of alloyed Pt_3Sn phase, the equation reported by Antolini and Gonzalez was used [16]:

$$y_{\text{Pt}_3\text{Sn}} = \frac{a - a_{\text{Pt}}}{a_{\text{Pt}_3\text{Sn}} - a_{\text{Pt}}}$$

Where $y_{\text{Pt}_3\text{Sn}}$ is the fraction of Pt_3Sn relative to the total platinum and a , $a_{\text{Pt}_3\text{Sn}}$ and a_{Pt} are the lattice parameters of the catalyst, the Pt and Pt_3Sn phases, respectively. Applying this equation, a 35% of Pt was estimated to be on Pt_3Sn form for the PtSn/C catalyst, while a value of 33% was obtained for the PtSn/TiCN catalyst. Therefore, if the catalysts reveal different catalytic performance toward the EOR, it should not be ascribed to the crystalline structure of the materials.

Fig. 2 shows representative TEM images, particle size distributions and the average particle size for both catalysts. It is to note, that TEM analysis provides “real” particle size, which is different to crystallite size achieved by XRD. PtSn nanoparticles supported on TiCN are

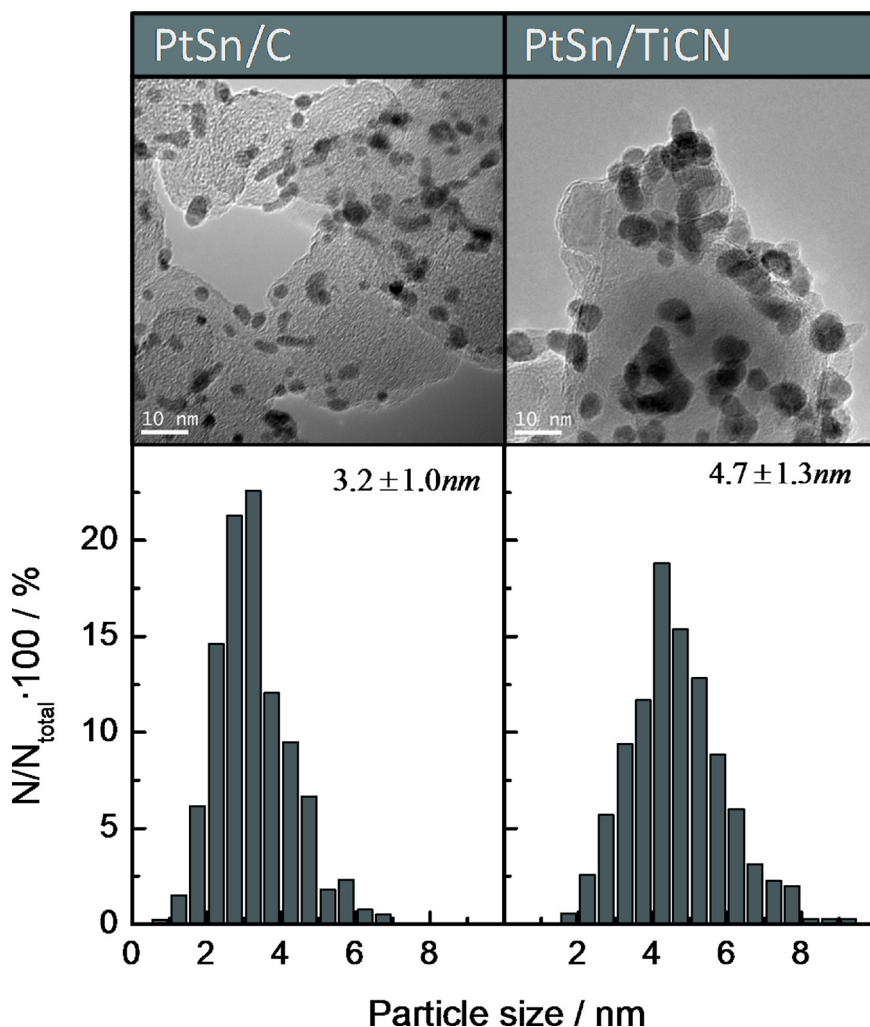


Fig. 2. Transmission electron micrographs and particle size distribution histograms of the catalysts.

slightly larger and more agglomerated than those supported on carbon Vulcan. In this regard, it is still not clear how particle size affects on the catalytic activity of platinum and platinum-tin nanoparticles toward the EOR, as not many systematic studies can be found in literature. Even it tends to be accepted that larger nanoparticles are more active toward the EOR [51–53], some works have reported higher activities for nanoparticles around 2–3 nm [54]. The dispersion on particle size can also affect both activity and selectivity of the catalysts [55]. The homogeneity of both samples is adequate, as can be observed at Fig. S1.

Table 1 summarizes some of the physicochemical properties of the two synthesized catalysts. Chemical analysis performed by inductively coupled plasma optical emission spectrometry (ICP-OES) reveals an

exact composition regarding both, platinum and tin contents. This is crucial in order to study the effect of the support, as different platinum and/or tin contents could strongly modify the catalytic activity. As overall, the PtSn nanoparticles obtained on both supports are quite similar in bulk chemical composition and crystalline structure. That means that the two synthesized catalysts are similar enough in terms of nanoparticles properties in order to be used for the purpose of studying the effect of the catalyst support on the EOR. Therefore, the differences observed in the catalytic activity toward the EOR for both catalysts will be ascribed mainly to the effect of the catalyst support.

Table 1 also presents data regarding surface chemical composition of the catalyst obtained by X-ray photoelectron spectroscopy (XPS).

Table 1
Physicochemical properties of the catalysts.

Metallic content (%)	Atomic ratio Pt:Sn	ICP-OES		XPS				Atomic ratio Pt:Sn	
		Pt 4f		Sn 3d					
		Pt 4f _{7/2} (eV)	Oxidation states contributions (%)	Sn 3d _{5/2} (eV)	Oxidation states contributions (%)				
PtSn/C	15	3:1	71.4	Pt(0): 71 Pt(II): 21 Pt(IV): 8	486.8	Sn(IV): 71 Sn (0): 29		1.3:1	
PtSn/TiCN	15	3:1	71.1	P(0): 78 Pt(II): 17 Pt(IV): 5	486.7	Sn(IV): 82 Sn(0): 18		0.9:1	

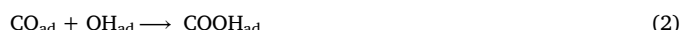
Deconvoluted spectra for Pt 4f, Ti 2p and Sn 3d core-levels are presented in the Supporting information (S2, S3, S4). PtSn/TiCN possesses slightly more reduced platinum and more oxidized tin than PtSn/C catalyst. The last could be related with the slightly lower alloy degree observed by XRD for the catalyst supported on titanium carbonitride, as the tin that is not forming the alloy, may be in the form of oxides. In addition, the amount of tin detected at the surface is considerably higher than that present on the bulk, and it is mainly detected as Sn^{4+} species, indicating the presence of SnO_2 on the surface. The last may have an important effect on the ethanol product selectivity, as the presence of tin on the surface has been associated to an increase of acetic acid yields and the suppression of the C–C cleavage and thus, CO_2 formation [15,18].

The more reduced state of platinum nanoparticles supported on titanium carbonitride than those supported on carbon was already reported previously [42]. The surface of the TiCN support is partially oxidized, as some peaks corresponding to TiO_2 are visible in the Ti 2p region, close to those peaks corresponding to reduced TiCN (S2). It is also important to note the significant shift to lower binding energies (BEs) of the Pt 4f peak at the titanium-based material in comparison to that revealed at the PtSn/C catalyst. The same behavior was observed for platinum nanoparticles supported on TiC, TiCN and TiN and indicates the presence of an electronic charge transfer from the titanium-based support to the PtSn nanoparticles [42]. This charge transfer was already predicted by DFT calculations for different transition metal clusters (including platinum) supported on TiC [56,57]. The presence of this charge transfer indicates that there is a strong interaction between the support and the metallic nanoparticles, which is expected to affect both, activity and stability [22]. In this sense, the BE value of the XPS Pt 4f peak was correlated with the CO tolerance at platinum supported on titanium-based materials, being more tolerant those catalysts that reveal lower BEs [42]. Even though a negative polarization of the platinum surface would be expected to hinder oxidation processes (as the catalyst has to take electrons from the reactant), it has been proposed that it contributes to the activation of OH groups in water [58,59]. Similar anti-correlations between BEs and catalytic activity toward CO and ethanol oxidation reactions have been reported for size-selected platinum clusters [58,60,61].

3.2. Spectroelectrochemical characterization

3.2.1. CO stripping

Carbon monoxide is a reaction intermediate during EOR, and it is also well-known that it is a strong catalyst poison. Therefore, its removal from the catalyst surface is a key factor to be investigated. Moreover, the CO oxidation reaction is an important tool to study the surface morphology and structure of the catalysts. It is widely accepted that the oxidation of CO_{ad} follows a Langmuir–Hinshelwood mechanism, in which the first reaction should be the formation of oxygenated species on the surface [62]:



Common strategies to enhance the CO tolerance are: i) increase the water dissociation reaction (1), ii) increase the CO surface diffusion (2), and iii) decrease the CO bond-dissociation energy.

Fig. 3 shows the CO stripping (red line) and the subsequent voltammogram (black line) for PtSn/TiCN and PtSn/C catalysts recorded at 0.02 V s^{-1} in acidic medium. The CO stripping profiles present a broad oxidation peak with an onset potential at ca. 0.3 V, which is typical for PtSn catalysts [13,16]. The anodic peak broadening should be ascribed to the CO oxidation at different active sites, e.g. adsorption of CO on diverse platinum sites with different adsorption strength. A close

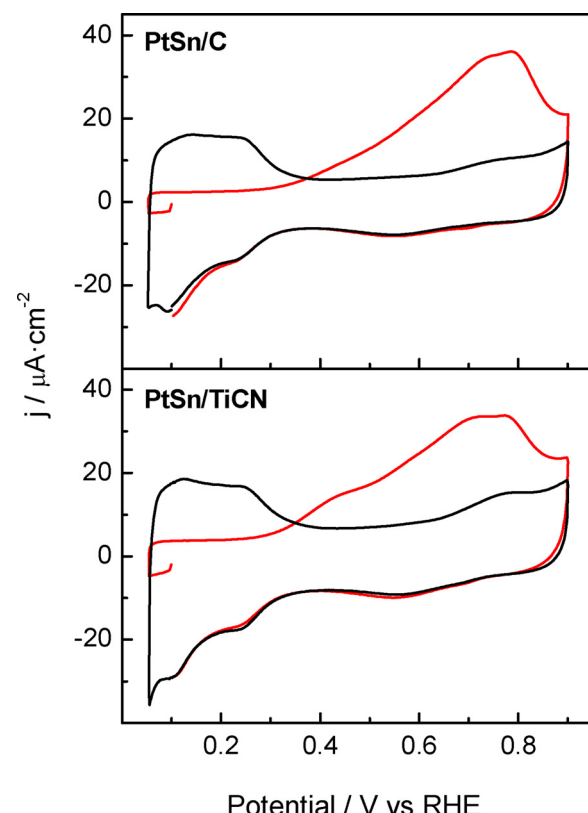


Fig. 3. CO stripping and subsequent blank voltammograms of the catalysts in $0.5 \text{ M H}_2\text{SO}_4$. Scan rate: 0.02 V s^{-1} .

inspection of the CO stripping profiles indicates higher CO tolerance for the Ti-based catalyst since a higher contribution of the anodic current at low overpotentials is discerned. Additionally, PtSn/TiCN catalyst develops an anodic shoulder at potentials close to 0.4 V and two main anodic peaks between 0.7 and 0.8 V. On the other hand, the anodic current developed by PtSn/C continuously increases up to 0.7–0.8 V, in which two anodic contributions are also discerned.

The described above is much clearer when the CO oxidation reaction is studied by DEMS, in which the $m/z = 44$ signal, that is associated to the formation of carbon dioxide, is followed (Fig. 4). It is important to note that in this case, data were recorded at slower scan rate (0.005 V s^{-1} instead of 0.02 V s^{-1}) that allows adsorbed CO to diffuse onto the catalyst surface in a larger extend and reach the most active site. Because of this, the anodic shoulder at 0.4 V recorded at 0.02 V s^{-1} at PtSn/TiCN becomes a clear anodic peak when the scan rate was 0.005 V s^{-1} . The high accuracy of the DEMS setup indicates similar onset potential (0.30 and 0.27 V for PtSn/C and PtSn/TiCN, respectively) for the CO oxidation on both catalysts. However, the CO_2 formation is much faster at the PtSn/TiCN material as can be clearly discerned in Fig. 4.

FTIR was employed in order to gain more insight of the mechanism of CO electrooxidation on PtSn/C and PtSn/TiCN catalysts. With this end in view, FTIR spectra were acquired by applying 0.1 V single potential steps from 0.1 V (R_0), in the positive going direction. Thus, positive and negative bands represent the loss and gain of species at the sampling potential, respectively. Additionally, a bipolar band means that an adsorbed species is still present at the surface and undergoes an important wavenumber shift as a consequence of increasing the potential. Fig. 5 shows a series of spectra acquired during the CO oxidation on PtSn/C (left panel) and PtSn/TiCN (right panel). The negative band at 2343 cm^{-1} is associated to the CO_2 formation and it is visible at $E \geq 0.50 \text{ V}$ for PtSn/C and at $E \geq 0.4 \text{ V}$ for PtSn/TiCN in agreement with previous results (Figs. 3 and 4). Linearly adsorbed CO (CO_l) is

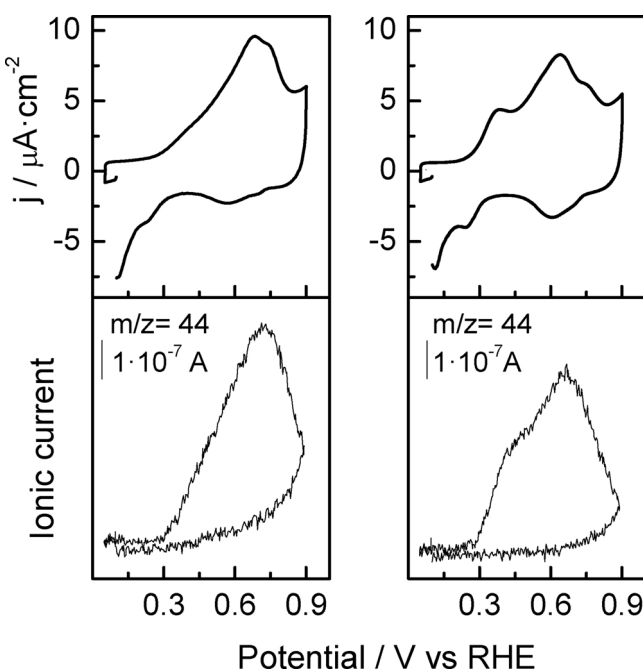


Fig. 4. Simultaneously recorded CO stripping voltammograms and $m/z = 44$ mass spectrometric cyclic voltammograms for PtSn/C (left) and PtSn/TiCN (right). 0.5 M H_2SO_4 . Scan rate: 0.005 V s^{-1} .

observed first as a signal that appears as bipolar at ca. $2080\text{--}2030 \text{ cm}^{-1}$ for both catalysts and turns positive at higher potentials for PtSn/C. As was described above, this particular behavior is associated to a species that is still adsorbed at the surface and suffers an important wavenumber shift as a consequence of increasing the applied potential [63].

Noticeable is the unusual behavior of this band at the PtSn/TiCN,

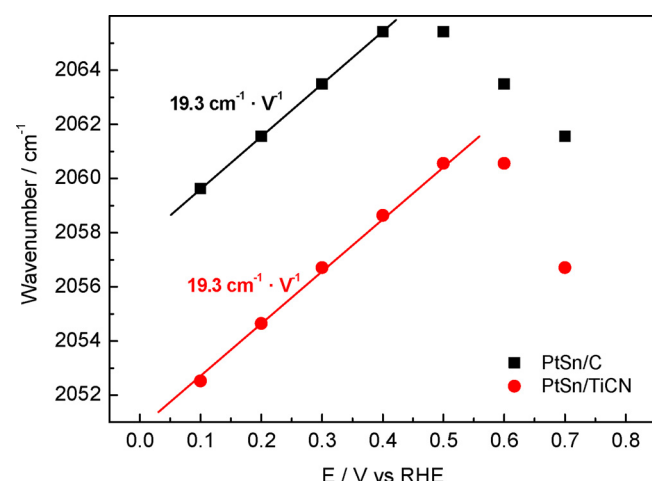


Fig. 6. Variation of the wavenumber of the CO band in front of the applied potential during the CO_{ads} oxidation experiment in 0.5 M H_2SO_4 followed by *in situ* FTIRs. Inset: PtSn/TiCN C–O band recorded at 0.2 V with an assignment of the two contributions.

which is not observed as an absolute positive band even at the highest potential applied. The latter is caused by the catalytic support (TiCN) that continuously produces active IR species (Ti–CO) in this wavenumber region at potentials higher than 0.2 V and makes confuse the band associated to the adsorbed CO on Pt [64,65]. In this context, TiCN not only develops this band in the current conditions, but also others associated to the vibrations between carbon, nitrogen and oxygen species (see SI and Figs. S6 and S7 for band assignment and for a deeper analysis). All the bands related to TiCN increase with the applied potential and most of them are associated to the water dissociation (adsorbed oxygenated species formation) on the surface of the catalyst support. It is noticeable that some of this bands appear as bipolar bands

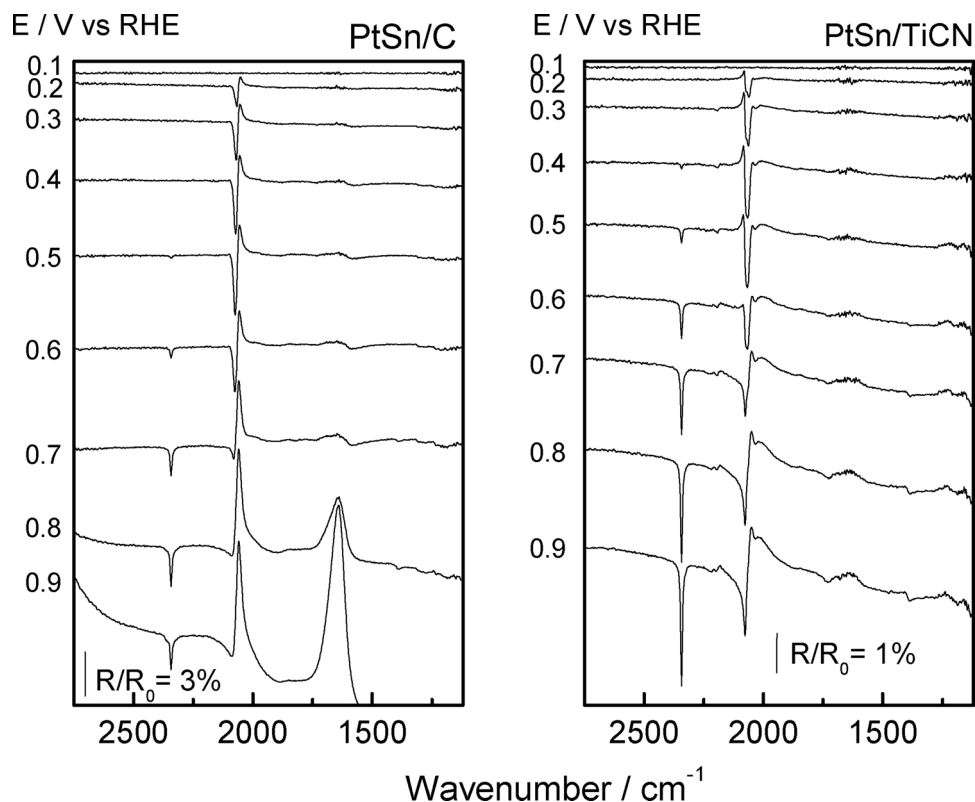


Fig. 5. *In situ* FTIR spectra corresponding to CO stripping on PtSn/C (left) and PtSn/TiCN (right). 0.5 M H_2SO_4 . R_0 = spectra at 0.1 V.

during the analysis of the PtSn/TiCN catalyst without CO (Fig. S6), indicating the facility in which the support is able to provide this oxygenated groups at low potentials.

Since a precise band centre value cannot be achieved from bipolar bands, the CO stripping spectra were recalculated with a new reference potential (0.9 V) where no CO_L is on the catalyst surface. In this way, absolute bands for PtSn/C and a better deconvolution of the bands associated to adsorbed CO on Pt and Ti for PtSn/TiCN were achieved. Fig. 6 depicts the band centre frequency shift for CO_L as function of the applied potential for both catalysts. Both catalysts develop a linear shift (Stark tuning) of the C–O stretch frequency with the voltage below 0.5 V. Interestingly, the tuning rate is the same for both material and similar to that reported for carbon-supported Pt catalyst, Pt/C ($20 \text{ cm}^{-1} \text{ V}^{-1}$) [63]. Having in mind that the tuning rate is typical for each system, the last results indicate that the change of the dipole moment of CO with the applied potential is the same for Pt/C, PtSn/C and PtSn/TiCN materials, while CO coverage and binding geometry are basically constant, and hence, CO only adsorbs on Pt.

Regarding to the wavenumber values of the CO_L band centers, a red shift is clearly visible for PtSn/TiCN in comparison to PtSn/C at the same potential range. The last clearly indicates that the CO adsorption binding energies and the vibration frequency in the absence of an electric field are affected by the catalytic support. Indeed, the lower wavenumber values achieved at PtSn/TiCN implies that the strength of the C–O bond decreases, or what is the same, the Pt–C binding energy increases. The latter is in completely agreement with the previous XPS analysis, in which the platinum surface was detected to be more negatively charged at PtSn/TiCN than at PtSn/C, and consequently, PtSn/TiCN is able to adsorb cations and neutral species more strongly.

After that, it is possible to summarize the principal outcomes of the CO stripping experiments. CO only adsorbs on Pt, meanwhile Sn and TiCN species provide oxygenated species (OH) at lower overpotential than Pt (bifunctional mechanism). Additionally, TiCN support weakens the C–O bond strength and consequently the reaction (2) and the CO tolerance are enhanced (electronic effect).

3.2.2. Ethanol oxidation

The electrochemical oxidation of ethanol at both catalysts was followed by cyclic voltammetry and by chronoamperometry techniques (Fig. 7). The left panel reveals that the voltammetric profiles are

similar. Indeed, both materials reveal analogous onset potential at ca. 0.3 V for the ethanol oxidation reaction. Even though the current density is similar for both catalyst at intermediate potentials (0.3–0.6 V in the positive scan), PtSn/TiCN develops higher current intensities at more positive potentials. The last is more evident at the right panel, where Tafel plots obtained from current transients at 600 s and different applied potentials are depicted. Thus, the EOR is enhanced at PtSn/TiCN during the potentiodynamic and potentiostatic experiments.

Fig. 7 depicts specific activities, thus, currents are normalized by the electrochemical surface area of the catalysts (estimation of catalytic active sites). The last is useful from an electrocatalytic and mechanistic point of view, as it shows the intrinsic activities of the materials. However, for a practical application on fuel cells, the mass activities are also important, as the amount of noble metal should also be taken into account. Fig. S5 shows cyclic voltammograms for the ethanol oxidation on both materials when current is normalized on the basis of platinum loading. In this case the activity for the PtSn/C catalyst is higher than for PtSn/TiCN. The last may be ascribed to the higher amount of Pt onto the surface of PtSn/C in comparison to PtSn/TiCN (see last column of Table 1). Accordingly, ESA values of 2.56 cm^2 and 8.42 cm^2 are achieved for PtSn/TiCN and PtSn/C, respectively.

Noticeable, the Tafel slope values are almost the same for both catalysts (0.265 V dec^{-1} for PtSn/TiCN and 0.263 V dec^{-1} for PtSn/C), which indicate similar reaction mechanism and rate determining step (RDS) of the EOR. The elevated slope value may be ascribed to an unsuitable surface for ethanol adsorption step (first step of the EOR) due to the high amount of surface oxide species [66,67]. So, the higher performance toward the EOR developed by the PtSn/TiCN material should be related to another reaction step.

In order to elucidate the reaction mechanism, *in situ* FTIRs was employed. FTIR spectra of the ethanol oxidation on both catalysts are depicted in Fig. 8. This figure reveals the typical IR bands that have already been reported in the literature for the ethanol oxidation on platinum and platinum-tin based catalysts [7,16,47,68,69]. Briefly, the positive bands at 2987 and 2908 cm^{-1} are associated to CH_3 and CH_2 groups from the ethanol consumption. Negative bands are related to species formation and they can be assigned in the subsequent way: 2343 cm^{-1} is related to CO_2 (O–C–O asym. str.); 2050 and 1850 cm^{-1} correspond to adsorbed CO on Pt in linear (CO_L str.) and bridge (CO_B str.) configuration, respectively; 1713 cm^{-1} can be associated to acetic

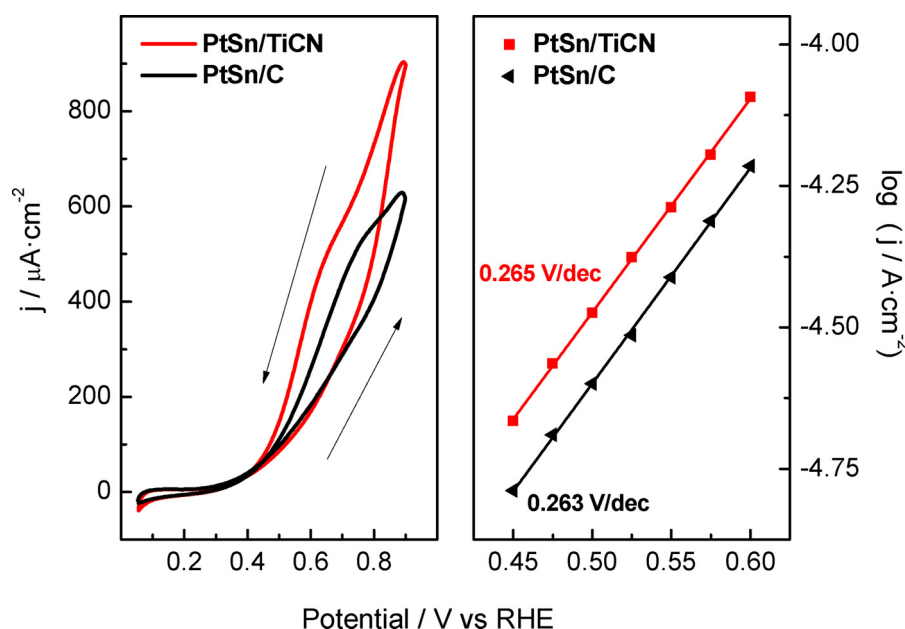


Fig. 7. Ethanol oxidation activities of the two catalysts in $2 \text{ M EtOH} + 0.5 \text{ M H}_2\text{SO}_4$. Left: cyclic voltammograms. Scan rate: 0.02 V s^{-1} . Right: Tafel plots obtained from 600 s current transients.

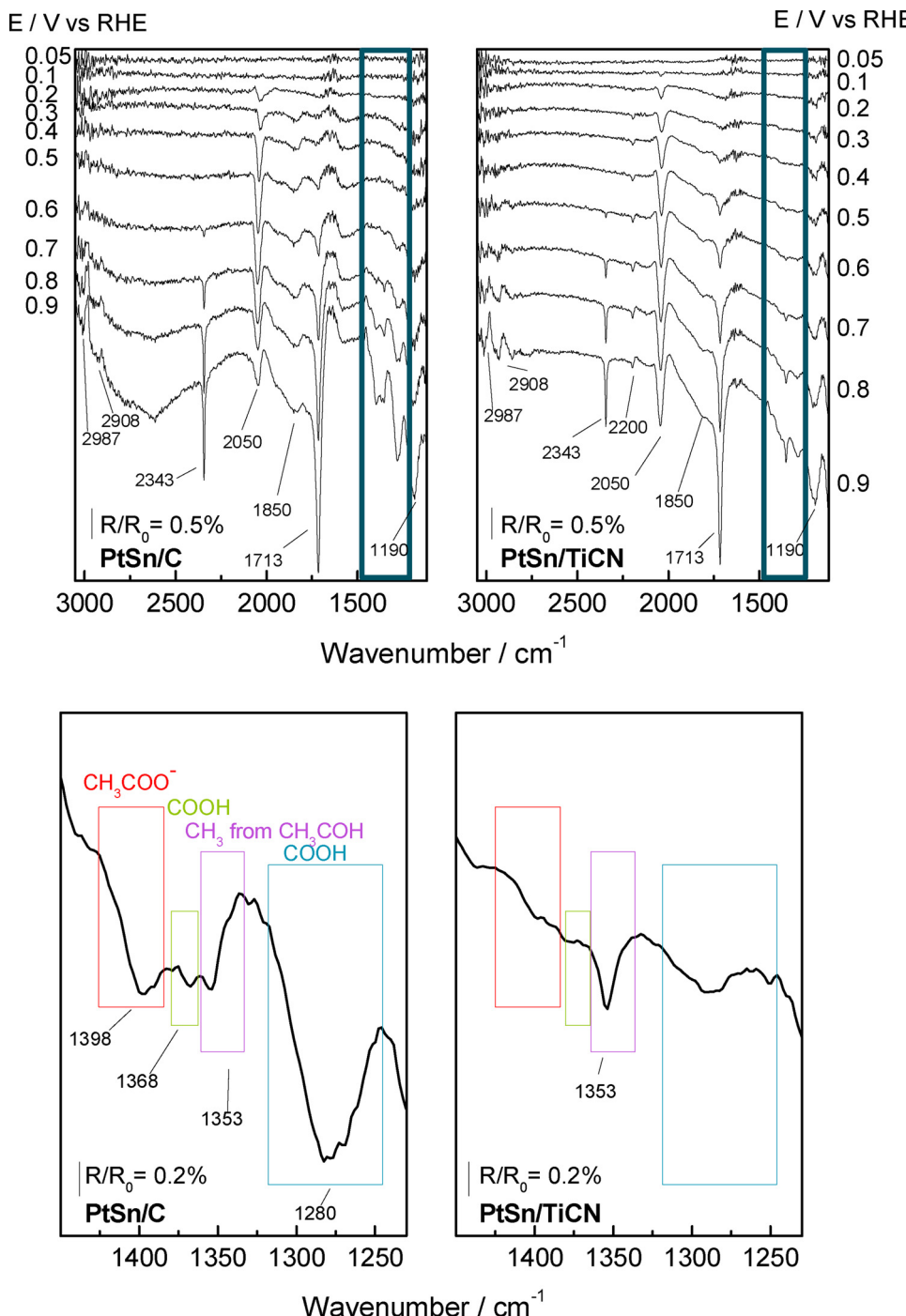


Fig. 8. Top panel: *In situ* FTIRs spectra of PtSn/C and PtSn/TiCN in 2 M EtOH + 0.5 M H₂SO₄. Low panel: amplification of the spectra at 0.9 V at the acetic acid signal region.

acid and/or acetaldehyde species (C=O str. of the carbonyl group); 1398 cm⁻¹ related to CH_3COO^- on Pt (C–O asym. C–O str.); 1368 and 1280 cm⁻¹ associated to acetic acid (coupled C–O str. + O–H def. on COOH group); 1353 cm⁻¹ correlated to acetaldehyde and/or acetic acid (sym. def. of the CH_3 group); 1190 cm⁻¹ linked to adsorbed sulfate species from the electrolyte; and the band at ca. 2200 cm⁻¹ is related to the TiCN support (N=C=O asym. str., see SI and Fig. S6).

Top-panels of Fig. 8 indicate that C–C cleavage occurs at 0.1 and 0.2 V at PtSn/TiCN and PtSn/C, respectively. However, CO₂ and carbonyl group (acetic acid and/or acetaldehyde species) formation take place at the same onset potential for both catalysts. Moreover, the intensities of the last bands are similar at both catalysts in the potential

range investigated, and accordingly, another species should be the source of the great difference between both materials in the catalytic activity toward the EOR. The DEMS analysis also revealed a similar amount of CO₂ and acetaldehyde formation (Fig. S8). A close inspection in the low-wavenumber region (bottom panels of Fig. 8) reveals the main differences between both catalysts during the EOR. At potentials higher than 0.5 V, PtSn/C shows bands associated to the formation of acetaldehyde, acetic acid and acetate [4,16], meanwhile PtSn/TiCN mainly displays the band related to the production of acetaldehyde.

This important difference in product selectivity between the two catalysts may explain the differences observed during the potentiodynamic and potentiostatic experiments (Fig. 7). In this regard, it is well-

known that acetate strongly adsorbs on platinum surfaces, decreasing the available number of active sites [4]. On the other hand, acetate is not formed on PtSn/TiCN and therefore active sites are available for further oxidation of ethanol to acetaldehyde. The last explains well the fact that the onset potential for the EOR, the Tafel slopes and the currents at small overpotentials are similar for both catalysts, while the current at potentials higher than 0.7 V (where strongly adsorbed acetate is already formed on PtSn/C) is much higher for the PtSn/TiCN catalyst.

As detected by XPS, the PtSn/TiCN surface is richer in tin oxides and higher acetic acid production than PtSn/C is expected (Table 1) [15]. However acetate/acetic acid at PtSn/TiCN was not detected and should, therefore, be related to geometric and diffusion factors of the TiCN catalyst support. Indeed, one of the main differences between carbon black and TiCN supports is their morphology. Carbon black (Vulcan XC-72R) is a highly porous carbon with micro and mesopores, meanwhile TiCN is constituted mainly by highly crystalline flat cubes. These different morphologies affect the diffusion behavior of reactants, intermediates and products of the alcohol oxidation reaction [70]. The accessible porous structure of carbon black favors the readorption of partially oxidized species (acetaldehyde) that will be further oxidized to acetate/acetic acid. On the other hand, the readorption of partially oxidized species at flat and smooth surfaces such as TiCN is low and consequently, the surface coverage by poisoning species (adsorbed acetate) decreases and the turnover frequency of ethanol increases.

4. Conclusions

Two catalysts were synthesized, made of platinum-tin nanoparticles supported on carbon black Vulcan and titanium carbonitride, respectively. Even the considerably different properties of the materials used as catalytic supports, similar platinum-tin nanoparticles were obtained on both catalysts (same chemical composition and alloying degree). In this way, the catalysts synthesized could be used to study the support effect on the catalytic properties toward CO and ethanol electrooxidation.

The first significant difference detected among the two catalysts was an important charge transfer from the TiCN support to the PtSn nanoparticles. This electronic effect was detected by both XPS and *in situ* FTIRs and involves a modification of the adsorption strengths of the different reactants and intermediates, which contributes to the enhancement of CO oxidation. However, it was also demonstrated by *in situ* FTIRs analysis that the surface of TiCN support was already covered with oxygenated species at low potentials. Thus, the support can also provide oxygenated species to the nanoparticles enhancing their reactivity toward the oxidation processes under study.

For the ethanol oxidation reaction, some interesting differences were also observed among both catalysts. PtSn/TiCN was reported to be considerably more active than PtSn/C, especially at higher potentials. *In situ* FTIRs revealed significant differences in the product selectivity. PtSn/TiCN catalyst does not produce any acetic acid. The last minimizes the platinum surface poisoning and, combined with the easy removal of CO adsorbed species, leads to an increase of the turnover frequency and, in turn, the activity toward the ethanol oxidation reaction.

In overall, it has been demonstrated that TiCN acts as a promoter support for PtSn nanoparticles toward the ethanol electrooxidation reaction. Several promotion mechanism, such as electronic interaction, bifunctional mechanism and geometric effects, have been reported to take place in the process.

Acknowledgements

This research was funded by Spanish Ministry of Economy and Competitiveness under projects ENE2014-52158-C2-1R and ENE2014-52158-C2-2R, and partially supported by the European Union Seventh Framework Programme via the EU project DECORE (project 309741)

under contract nº FP7-NMP-2012-SMALL-6 for Research and Technological Development. MR acknowledges the FPU-2012 program for financial support. GG acknowledges the Viera y Clavijo program (ACIISI & ULL) for financial support.

Appendix A. Supplementary data

Supplementary material related to this article can be found, in the online version, at doi:<https://doi.org/10.1016/j.apcatb.2018.05.078>.

References

- [1] F. Vigier, S. Rousseau, C. Coutanceau, J.-M. Leger, C. Lamy, *Top. Catal.* 40 (2006) 111–121.
- [2] A. Rabis, P. Rodriguez, T.J. Schmidt, *ACS Catal.* 2 (2012) 864–890.
- [3] L. An, T.S. Zhao, Y.S. Li, *Renew. Sustain. Energy Rev.* 50 (2015) 1462–1468.
- [4] S.C.S. Lai, M.T.M. Koper, *Faraday Discuss.* 140 (2009) 399–416.
- [5] M.T.M. Koper, S.C. Lai, E. Herrero, M.T.M. Koper (Ed.), *Fuel Cell Catalysis: A Surface Science Approach*, John Wiley & Sons, Inc., 2009.
- [6] T. Iwasita, E. Pastor, *Electrochim. Acta* 39 (1994) 531–537.
- [7] A. Rodes, E. Pastor, T. Iwasita, *J. Electroanal. Chem.* 376 (1994) 109–118.
- [8] J.M. Orts, R. Gómez, J.M. Feliu, A. Aldaz, J. Clavilier, *Electrochim. Acta* 39 (1994) 1519–1524.
- [9] T.S. Almeida, A.R. Van Wassen, R.B. VanDover, A.R. de Andrade, H.D. Abruna, *J. Power Sources* 284 (2015) 623–630.
- [10] N. Erini, S. Rudi, V. Beermann, P. Krause, R. Yang, Y. Huang, P. Strasser, *ChemElectroChem* 2 (2015) 903–908.
- [11] A. Kowal, M. Li, M. Shao, K. Sasaki, M.B. Vukmirovic, J. Zhang, N.S. Marinkovic, P. Liu, A.I. Frenkel, R.R. Adzic, *Nat. Mater.* 8 (2009) 325–330.
- [12] G. García, N. Tsiorvaras, E. Pastor, M.A. Peña, J.L.G. Fierro, M.V. Martínez-Huerta, *Int. J. Hydrogen Energy* 37 (2012) 7131–7140.
- [13] S.C. Zignani, V. Baglio, E.R. Gonzalez, A.S. Arico, *ChemElectroChem* 1 (2014) 1403–1406.
- [14] L.S. Parreira, J.C.M. Silva, F.R. Simões, M.A.L. Cordeiro, R.H. Sato, E.R. Leite, M.C. dos Santos, *ChemElectroChem* 4 (2017) 1950–1958.
- [15] E. Antolini, E.R. Gonzalez, *Catal. Today* 160 (2011) 28–38.
- [16] F. Vigier, C. Coutanceau, F. Hahn, E.M. Belgsir, C. Lamy, *J. Electroanal. Chem.* 563 (2004) 81–89.
- [17] E. Antolini, E.R. Gonzalez, *Electrochim. Acta* 55 (2010) 6485–6490.
- [18] R. Rizo, M.J. Lázaro, E. Pastor, G. García, *Molecules* 21 (2016) 1225.
- [19] M. Murawska, J.A. Cox, K. Miecznikowski, J. Solid State Electrochem.: Curr. Res. Dev. Sci. Technol. 18 (2014) 3003–3010.
- [20] I.A. Rutkowska, M.D. Koster, G.J. Blanchard, P.J. Kulesza, *J. Power Sources* 272 (2014) 681–688.
- [21] H. Wang, Q. Ma, *J. Electrochem. Soc.* 161 (2014) F1202–F1207.
- [22] Y. Liu, T.G. Kelly, J.G. Chen, W.E. Mustain, *ACS Catal.* 3 (2013) 1184–1194.
- [23] G. García, O. Guillén-Villaflor, J.L. Rodríguez, M.C. Arévalo, E. Pastor, *Int. J. Hydrogen Energy* 41 (2016) 19664–19673.
- [24] M.V. Martínez-Huerta, M.J. Lázaro, *Catal. Today* 285 (2017) 3–12.
- [25] L. Xiong, L. Zheng, C. Liu, L. Jin, Q. Liu, J. Xu, *J. Electrochem. Soc.* 162 (2015) F468–F473.
- [26] L. Yang, Y.C. Kimmel, Q. Lu, J.G. Chen, *J. Power Sources* 287 (2015) 196–202.
- [27] Z. Li, B. Li, Z. Liu, Z. Liu, D. Li, *RSC Adv.* 5 (2015) 94495–94499.
- [28] X. Ma, H. Meng, M. Cai, P.K. Shen, *J. Am. Chem. Soc.* 134 (2012) 1954–1957.
- [29] T. Huang, S. Mao, G. Zhou, Z. Zhang, Z. Wen, X. Huang, S. Ci, J. Chen, *Nanoscale* 7 (2015) 1301–1307.
- [30] L. Lin, W. Sheng, S. Yao, D. Ma, J.G. Chen, *J. Power Sources* 345 (2017) 182–189.
- [31] Z. Yan, L. Gao, M. Zhang, J. Xie, M. Chen, *RSC Adv.* 5 (2015) 9561–9564.
- [32] J.A. Rodriguez, F. Vines, F. Illas, P. Liu, Y. Takahashi, K. Nakamura, *J. Chemical Phys.* 127 (2007) 211102.
- [33] Y. Peng, H. Miao, Z. Peng, *Int. J. Refract. Met. Hard Mater.* 39 (2013) 78–89.
- [34] Y. Xiao, G. Zhan, Z. Fu, Z. Pan, C. Xiao, S. Wu, C. Chen, G. Hu, Z. Wei, *Electrochim. Acta* 141 (2014) 279–285.
- [35] M.M.O. Thotiyil, S. Sampath, *Electrochim. Acta* 56 (2011) 3549–3554.
- [36] Y. Ou, X. Cui, X. Zhang, Z. Jiang, *J. Power Sources* 195 (2010) 1365–1369.
- [37] M.M. Ottakam Thotiyil, T. Ravikumar, S. Sampath, *J. Mater. Chem.* 20 (2010) 10643.
- [38] K. Kakinuma, Y. Wakasugi, M. Uchida, T. Kamino, H. Uchida, S. Deki, M. Watanabe, *Electrochim. Acta* 77 (2012) 279–284.
- [39] A. Ignaszak, C. Song, W. Zhu, J. Zhang, A. Bauer, R. Baker, V. Neburchilov, S. Ye, S. Campbell, *Electrochim. Acta* 69 (2012) 397–405.
- [40] C. Rüdiger, J. Brumbarov, F. Wiesinger, S. Leonardi, O. Paschos, C.V. Vidal, J. Kunze-Liebhäuser, *ChemCatChem* 5 (2013) 3219–3223.
- [41] D.T. Dam, K.-D. Nam, H. Song, X. Wang, J.-M. Lee, *Int. J. Hydrogen Energy* 37 (2012) 15135–15139.
- [42] M. Roca-Ayats, G. García, J.L. Galante, M.A. Peña, M.V. Martínez-Huerta, *J. Phys. Chem. C* 117 (2013) 20769–20777.
- [43] M. Roca-Ayats, E. Herreros, G. García, M.A. Peña, M.V. Martínez-Huerta, *Appl. Catal. B: Environ.* 183 (2016) 53–60.
- [44] M. Roca-Ayats, G. García, M. Soler-Vicedo, E. Pastor, M.J. Lázaro, M.V. Martínez-Huerta, *Int. J. Hydrogen Energy* 40 (2015) 14519–14528.
- [45] M. Roca-Ayats, G. García, M.A. Peña, M.V. Martínez-Huerta, *J. Mater. Chem. A* 2

(2014) 18786–18790.

[46] C. Bock, C. Paquet, M. Couillard, G.A. Botton, B.R. MacDougall, *J. Am. Chem. Soc.* 126 (2004) 8028–8037.

[47] T. Iwasita, F.C. Nart, *Prog. Surf. Sci.* 55 (1997) 271–340.

[48] O. Guillén-Villafuerte, G. García, M.C. Arévalo, J.L. Rodríguez, E. Pastor, *Electrochim. Commun.* 63 (2016) 48–51.

[49] J.M. Guilemany, I. Sanchiz, X. Alcobé, *Powder Diffr.* 7 (1992) 34–35.

[50] P.E. Tsiakaras, *J. Power Sources* 171 (2007) 107–112.

[51] S. St John, P. Boolchand, A.P. Angelopoulos, *Langmuir: ACS J. Surf. Colloids* 29 (2013) 16150–16159.

[52] E.A. Baranova, A. Tavasoli, T. Amir, *Electrocatalysis* 2 (2011) 89.

[53] M.T. Koper, *Nanoscale* 3 (2011) 2054–2073.

[54] J. Perez, V.A. Paganin, E. Antolini, *J. Electroanal. Chem.* 654 (2011) 108–115.

[55] J. Gomes, D. Profeti, L.J. Deiner, *ChemElectroChem* 1 (2014) 655–662.

[56] T. Gomez, E. Florez, J.A. Rodriguez, F. Illas, *J. Phys. Chem. C* 115 (2011) 11666–11672.

[57] J. Mao, S. Li, X. Chu, Z. Yang, *J. Appl. Phys.* 118 (2015) 185301.

[58] A. von Weber, E.T. Baxter, S. Proch, M.D. Kane, M. Rosenfelder, H.S. White, S.L. Anderson, *Phys. Chem. Chem. Phys.* 17 (2015) 17601–17610.

[59] M. Neurock, First-principles modeling for the electro-oxidation of small molecules, in: W. Vielstich, A. Lamm, H.A. Gasteiger, H. Yokokawa (Eds.), *Handbook of Fuel Cells*, John Wiley & Sons, 2010.

[60] S. Proch, M. Wirth, H.S. White, S.L. Anderson, *J. Am. Chem. Soc.* 135 (2013) 3073–3086.

[61] F.S. Roberts, M.D. Kane, E.T. Baxter, S.L. Anderson, *Phys. Chem. Chem. Phys.* 16 (2014) 26443–26457.

[62] S. Gilman, *J. Phys. Chem.* 68 (1964) 70–80.

[63] G. García, J.A. Silva-Chong, O. Guillén-Villafuerte, J.L. Rodríguez, E.R. González, E. Pastor, *Catal. Today* 116 (2006) 415–421.

[64] B.H. Stuart, *Infrared Spectroscopy: Fundamentals and Applications*, Wiley, 2004.

[65] R.D. Cowling, H.E. Hintermann, *J. Electrochem. Soc.* 118 (1971) 1912–1916.

[66] S.-Y. Yan, Y.-R. Huang, C.-Y. Yang, C.-W. Liu, J.-H. Wang, K.-W. Wang, *Electrochim. Acta* 259 (2018) 733–741.

[67] A. Velázquez-Palenzuela, E. Brillas, C. Arias, F. Centellas, J.A. Garrido, R.M. Rodríguez, P.-L. Cabot, *J. Power Sources* 225 (2013) 163–171.

[68] T. Iwasita, B. Rasch, E. Cattaneo, W. Vielstich, *Electrochim. Acta* 34 (1989) 1073–1079.

[69] B. Rasch, T. Iwasita, *Electrochim. Acta* 35 (1990) 989–993.

[70] G.A. Planes, G. García, E. Pastor, *Electrochim. Commun.* 9 (2007) 839–844.